

Theoretical study of the line profiles of the hydrogen perturbed by collisions with protons

M. G. Santos^{1*} and S. O. Kepler¹

¹*Instituto de Física, Universidade Federal do Rio Grande do Sul, 91501-900 Porto Alegre, RS, Brazil*

Accepted 2012 January 24. Received 2012 January 17; in original form 2011 September 22

ABSTRACT

We present theoretical calculations of the quasi-molecular line profiles for the Lyman ($\text{Ly}\alpha$, $\text{Ly}\beta$, $\text{Ly}\gamma$, $\text{Ly}\delta$) and Balmer ($\text{H}\alpha$, $\text{H}\beta$, $\text{H}\gamma$, $\text{H}\delta$, $\text{H}\epsilon$, $\text{H}8$, $\text{H}9$, and $\text{H}10$) series, perturbed by collisions with protons. In all calculations we include the dependence of the dipole moments as a function of internuclear distance during the collision. The broadening from ion collisions must be added to the normal electron Stark broadening.

Key words: white dwarf, line profiles, collision broadening.

1 INTRODUCTION

The satellite lines present in the far wing profiles of the Lyman and Balmer series lines of atomic hydrogen have been observed in stars and in laboratory plasmas (Kielkopf et al. 2002). Experimentally, the primary difficulties in studying these line profiles are (1) the development of techniques to observe neutral atomic hydrogen interactions at densities high enough for spectral line broadening effects to be significant, and (2) quantitatively characterizing the conditions under which the spectra are created. On the theoretical side, the difficulty arises in developing methods for computing the contributions from all possible molecular states of H_2 and H_2^+ to the spectrum of free atoms in collision.

Satellite features at 1600 Å and 1405 Å in the Lyman- α wing associated with free-free quasi-molecular transitions of H_2 and H_2^+ are observed in the ultraviolet (UV) spectra of a few stars obtained with the International Ultraviolet Explorer (IUE) and the Hubble Space Telescope (HST). The satellites in the red wing of Lyman- β are in the 905 to 1187 Å spectral region, covered by Far Ultraviolet Spectroscopic Explorer (FUSE). The stars which show Lyman satellites are DA white dwarfs (WDs), old Horizontal Branch stars of spectral type A, and λ Bootis stars (Allard et al. 2000). WDs are the end product of evolution of $\sim 98\%$ of all stars (e.g., Kepler et al. 2007). Having consumed all available nuclear fuel (which depends on the individual stellar mass), their source of luminosity is dominated by only the residual internal thermal energy. This radiates away, exponentially cooling the star, but due to the small surface area (a typical WD radius is $\sim 10^9$ cm), cooling times are long, taking approximately 10^{10} years for their effective temperatures to decrease from around 10^5 K to near 10^3 K.

Therefore, WDs are old, and hidden in their structure is a historical record of stellar formation and evolution in our Galaxy.

UV spectroscopic observations of WDs reveal a line shape very different from the expected simple Stark broadening, with satellite lines in the red wing of Lyman- β near 1078 and 1060 Å (Koester et al. 1996, 1998). The strengths of these satellite features, and indeed the entire shape of the wings in the Lyman series, are very sensitive to the degree of ionization in the stellar atmosphere or laboratory plasma, because it is the ionization that determines the relative importance of broadening by ion and neutral collisions. Therefore the satellites may be used as a temperature diagnostic in a plasma where Saha ionization-equilibrium holds. In the case of Lyman- α and the H - H^+ Lyman- β satellites, the shape of the potential plays a dominant role in the large difference in the broadening of quasi-molecular features (Allard et al. 1998b).

Quasi-molecular transitions occur when a photon is absorbed or emitted by a hydrogen atom while this atom interacts with one or more neighboring particles, which may be atoms, ions or molecules (Allard & Kielkopf 1982). At short distances, the interaction between the perturbed atoms and the other particle(s) usually leads to the formation of satellite molecular lines on the wings of atomic lines (Allard et al. 1998a,b, 1999). Structures observed in the wing of Lyman- α at 1623 Å and 1405 Å are due to absorptions of quasi-molecular H_2 and H_2^+ , respectively. The intensity of these two satellites depends strongly on the degree of ionization in the stellar atmosphere and consequently on the effective temperature T_{eff} and surface gravity $\log g$ (Holweger et al. 1994).

The atmosphere of a WD comprises less than 10^{-13} of the stellar mass and is dominated by hydrogen (DA white dwarfs) or helium (DB/DO) and sometimes shows small

* E-mail: marcios@if.ufrgs.br

amounts of heavy elements (e.g., DAZ, DBZ and DOZ white dwarfs) (see, e.g., Koester 2010). The primary technique to determine T_{eff} and $\log g$ of WDs is by comparing observed spectra with synthetic spectra from theoretical atmosphere models (e.g., Tremblay et al. 2009). The advantage of this spectroscopic technique is that the theoretical line profiles are extremely sensitive to variations in the atmospheric parameters. Bergeron et al. (1992) were one of the first to apply this to a large number of WDs; they fit the hydrogen Balmer lines. The technique was later applied to the UV Lyman lines (e.g., Bergeron et al. 1995; Kepler et al. 1993; (2005)).

Bergeron et al. (2002) made improvements to the models by taking into account the optical quasi-molecular opacities due to the dipole moments induced by the interaction between particles. This interaction causes a temporary rearrangement of electronic charges, which forms a temporary molecule, thus producing absorptions or emissions beyond those of the isolated atoms.

Currently there are a large number of optical spectra of WDs that have been taken as part of the Sloan Digital Sky Survey (SDSS) (e.g., Eisenstein et al. 2006; Kleinman et al. 2010), allowing for the study of the WD mass distribution (Kepler et al. 2007). Kleinman et al. (2004) and Liebert et al. (2005) derive masses from spectroscopic fits, and Bergeron et al. (1991) and Koester (1991) discuss the apparent increase in the average mass of DAs with $T_{\text{eff}} < 12\,000$ K. Kepler et al. (2006) compare SDSS spectra with high S/N spectra obtained with the 8 m Gemini telescope for four WDs with $T_{\text{eff}} \sim 12\,000$ K and determine that the masses derived from fitting the relatively low S/N SDSS spectra are systematically overestimated by $\Delta M \simeq 0.13 M_{\odot}$. Due to a correlation between T_{eff} and $\log g$ (a small increase in T_{eff} can be offset by a small decrease in $\log g$), such discrepancies are concentrated only in the region around the maximum of the Balmer lines, $14\,000 \text{ K} \geq T_{\text{eff}} \geq 12\,000 \text{ K}$. To study the trend of the apparent increased average mass of DAs, Kepler et al. (2010) analyse 1505 such WDs with $S/N \geq 20$ and $T_{\text{eff}} > 12\,000 \text{ K}$ and determined an average DA mass of $M/M_{\odot} = 0.604 \pm 0.003$. They observe that the distribution of the sample is similar to that of the Palomar Green survey published by Liebert et al. (2005). Falcon et al. (2010) used an ensemble average of gravitational redshifts of 449 DAs, which is independent of line profiles, and estimated a mean mass of $0.640 \pm 0.014 M_{\odot}$.

Koester et al. (2009), Koester (2010), Tremblay et al. (2009) and Gianninas et al. (2010) study the possible causes for this apparent increase in mass, not seen in photometric determinations (Engelbrecht & Koester 2007; Kepler et al. 2007). They conclude this phenomenon is not caused by He contamination, but Tremblay et al. (2011) propose that the use of one-dimensional calculations of convection in the atmosphere, compared to more realistic three-dimensional calculations, might be the cause. There is a huge effort to eliminate the inconsistencies in the model calculations, and these attempts show the need for continued study of the interaction of hydrogen perturbed by protons, electrons, atoms and molecules at high pressure.

The goal of our work is the study of the interaction of the hydrogen atom with protons, which temporarily creates the molecule H_2^+ . We calculate the potential of H_2^+ up to $n = 10$, and analyze all possible transitions that can occur,

as well as the dipole moments for all possible transitions. In the literature, we find calculations for only $\text{Ly}\alpha$, $\text{Ly}\beta$ and $\text{Ly}\gamma$ and $\text{H}\alpha$; for these, we calculate to increased resolution. This new theoretical data must be inserted in the modeling of line profiles at high density, in addition to the electron Stark broadening.

2 THEORETICAL ANALYSIS

The dipole moments induced by the interaction between radiator and perturber cause a temporary repositioning of electronic charges, which temporarily forms a molecule. This leads to the possible appearance of satellite features in the wing of the line profile and produces different absorptions or emissions than those of non-interacting atoms (Frommhold 1993).

The position of the satellite line depends directly on the extreme of the potential difference of the transition $\Delta V_{\text{ext}}(R)$ and the dependence of the potential difference $\Delta V(R) = V_j(R) - V_i(R)$ with internuclear separation R of the states i and j of the allowed transitions of the H_2^+ ; the intensity and shape of the satellites depend on both the potential difference and the radiative dipole moment (Allard et al. 2004).

To calculate spectral line profiles, affected by collisions with protons, we must know precisely the theoretical potential that describes the molecular interaction between radiator and perturber, as well as the changes in dipole momenta due to the radioactive atom-ion separation for each molecular state.

Madsen & Peek (1971) calculate the values of the potential of H_2^+ only for states with $n \leq 3$. Allard et al. (2004) calculate the potential for states with $n \leq 4$, which allows them to calculate the line profile for Lyman- γ .

The values of the dipole moments of H_2^+ that are available in the literature were calculated by Ramaker & Peek (1972, 1973), and Allard et al. (2009) refers to the calculation of $n = 4$.

For this paper, we calculate all potential and dipole moments up to $n \leq 10$ of H_2^+ as a function of the internuclear distance R up to 300 a.u. (atomic units), with a step of 0.01 a.u. We compare the potential of the $n \leq 3$ states with those in the literature (Madsen & Peek 1971) and show differences smaller than 10^{-13} , the precision quoted in the published values. We also compare the computed dipole moments with those tabulated by Ramaker & Peek (1973) and those plotted in Allard et al. (2009); they are fully consistent.

2.1 Potentials for the Hydrogen Molecule H_2^+

The structure of the molecular ion H_2^+ has been studied by Teller (1930), Hylleraas (1931), Jaffé (1934), Baber & Hassé (1935), Bates & Poots (1953), and Madsen & Peek (1971), but accurate tables of the electronic energy as a function of internuclear distance for the excited states $n \geq 3$ have not been published.

As originally shown by Burrau (1927), the Schrödinger equation for H_2^+ can be separated and the electronic energy E calculated exactly. The Schrödinger equation of the elec-

tron in atomic units is:

$$\frac{1}{2}\nabla^2\Psi + \left(E + \frac{1}{r_a} + \frac{1}{r_b} - \frac{1}{R}\right)\Psi = 0 \quad (1)$$

where r_a and r_b are the distances measured in units of a_0 of the electron to the two positive charges a and b , E is the energy measured in units of Hartree E_h , and R is the internuclear separation.

In terms of confocal elliptical coordinates, defined by: $\lambda = (r_a + r_b)/R$, $\mu = (r_a - r_b)/R$ and ϕ , the azimuthal angle with respect to the internuclear axis, the Schrödinger equation can then be separated in three equations:

$$\frac{\partial^2\Phi}{\partial\phi^2} + m^2\Phi = 0 \quad (2)$$

$$\frac{\partial}{\partial\mu} \left[(1 - \mu^2) \frac{\partial M}{\partial\mu} \right] + \left(-A + p^2\mu^2 - \frac{m^2}{1 - \mu^2} \right) M = 0 \quad (3)$$

and

$$\frac{\partial}{\partial\lambda} \left[(\lambda^2 - 1) \frac{\partial \Lambda}{\partial\lambda} \right] + \left(A + 2R\lambda - p^2\lambda^2 - \frac{m^2}{\lambda^2 - 1} \right) \Lambda = 0 \quad (4)$$

where $\Psi(\lambda, \mu, \phi) = \Lambda(\lambda)M(\mu)\Phi(\phi)$, $p^2 = \frac{-\varepsilon R^2}{2}$, $\varepsilon = E - \frac{1}{R}$ is the electronic energy, and where A and m are the constants of separation.

The solution of equation (2) is direct, i. e.:

$$\Phi = e^{(\pm im\phi)}. \quad (5)$$

The solution of equation (3), the angular component, is obtained using the Hylleraas (1931) method:

$$M(\mu) = \sum_s c_s P_{m+s}^m(\mu), \quad (6)$$

where $P_{m+s}^m(\mu)$ are the generalized Legendre polynomials of first order. The summation extends only over even or odd values of s , depending on the state calculated.

Applying equation (6) in equation (3), we obtain a recurrence relation for the coefficients c_s ,

$$a_s c_{s-2} + b_s c_s + d_s c_{s+2} = 0 \quad (7)$$

where:

$$a_s = p^2 \frac{(s-1)s}{(2s+2m-3)(2s+2m-1)}$$

$$b_s = -A - (s+m)(s+m+1) +$$

$$+ p^2 \left[\frac{(s+1)(s+1+2m)}{(2s+2m+3)(2s+2m+1)} + \frac{s(s+2m)}{(2s+2m+1)(2s+2m-1)} \right]$$

$$d_s = p^2 \frac{(s+2m+2)(s+2m+1)}{(2s+2m+5)(2s+2m+3)}$$

The recurrence relation (7) forms an infinite set of homogeneous linear equations whose solution requires the determinant of the coefficient matrix to be null.

The solution of equation (4) for the radial part is obtained using the method of Jaffé (1934).

$$\Lambda(\lambda) = (\lambda^2 - 1)^{\frac{m}{2}} (1 + \lambda)^\sigma e^{-p\lambda} \sum_{t=0}^{\infty} g_t \left(\frac{\lambda - 1}{\lambda + 1} \right)^t, \quad (8)$$

where $\sigma = \frac{R}{p} - m - 1$.

Applying equation (8) to the equation (4), the following recurrence equation is found:

$$\alpha_t g_{t+1} - \beta_t g_t + \gamma_t g_{t-1} = 0. \quad (9)$$

where:

$$\alpha_t = (t+1)(t+m+1),$$

$$\beta_t = 2t^2 + (4p - 2\sigma)t - A + p^2 - 2p\sigma - (m+1)(m+\sigma),$$

$$\gamma_t = (t-1-\sigma)(t-1-\sigma-m).$$

The recurrence relation (9) also produces an infinite set of homogeneous linear equations, whose determinant of the matrix of coefficients must also be null. When calculating the determinant of the infinite recurrence relations of equations (7) and (9), we obtain two functions $f_1(A, \varepsilon, R)$ and $f_2(A, \varepsilon, R)$ which depend on A , ε , and R . The electronic energy (potential energy V_i) ε is obtained by calculating the solution of both functions $f_1(A, \varepsilon, R)$ and $f_2(A, \varepsilon, R)$, e.g., by using the Newton-Raphson method. Practical considerations require the truncation of the recurrence relations (9) and (7). We choose $t=s=25$ for the data presented here, because larger values for t and s do not produce any significant change in A and ε . The coefficients c_s and g_t are calculated using the method of continued fractions.

2.2 Electric dipole moments

Choosing the origin of the coordinate system in the center of the line segment which unites the two positive charges and taking this line as the axis z , the matrix element to be evaluated of the components of the electric dipole moment, D_{ij} , specified by:

$$D_{ij} = e \langle i | \mathbf{r} | j \rangle = e Q_{i,j}(\mathbf{r}), \quad (10)$$

where e represents the electron charge, \mathbf{r} is the position vector of the electron relative to molecular fixed frame, in coordinates x , y and z of the electron, Ψ_i and Ψ_j are the electronic functions in the Born-Oppenheimer approximation of the states i and j and $Q_{i,j}(\mathbf{r})$ the matrix elements.

The matrix elements $Q_{i,j}(\mathbf{r})$ of the various components of the electric dipole moment according to Ramaker & Peek (1973), are specified by:

$$Q_{i,j}(\mathbf{r}) = \int \Psi_i^*(\lambda, \mu, \phi)(\mathbf{r}) \Psi_j(\lambda, \mu, \phi) d\tau. \quad (11)$$

where τ is the volume element. $Q_{i,j}(\mathbf{r})$ is obtained by inserting the equations (5), (6) and (8) into equation (11). The matrix elements $Q_{i,j}(\mathbf{r})$ can be written as a function of the coordinates x , y and z as follows:

$$Q_{i,j}(x) = N_i N_j \left(\frac{R}{2} \right)^4 \int_0^{2\pi} \Phi_i^*(\phi) \cos(\phi) \Phi_j(\phi) d\phi \times \left[\Omega_{i,j} \left(\frac{1}{2}, 0, \frac{1}{2}, 2 \right) - \Omega_{i,j} \left(\frac{1}{2}, 2, \frac{1}{2}, 0 \right) \right] \quad (12)$$

$$Q_{i,j}(y) = N_i N_j \left(\frac{R}{2} \right)^4 \int_0^{2\pi} \Phi_i^*(\phi) \sin(\phi) \Phi_j(\phi) d\phi \times \left[\Omega_{i,j} \left(\frac{1}{2}, 0, \frac{1}{2}, 2 \right) - \Omega_{i,j} \left(\frac{1}{2}, 2, \frac{1}{2}, 0 \right) \right] \quad (13)$$

$$Q_{i,j}(z) = N_i N_j \left(\frac{R}{2} \right)^4 \int_0^{2\pi} \Phi_i^*(\phi) \Phi_j(\phi) d\phi \times [\Omega_{i,j}(0, 1, 0, 3) - \Omega_{i,j}(0, 3, 0, 1)] \quad (14)$$

where $\Omega_{i,j}(a, b, c, d)$ is defined by:

$$\Omega_{i,j}(a, b, c, d) = \int_{-1}^1 M_i^*(\mu)(1 - \mu^2)^a \mu^b M_j(\mu) d\mu \times \int_1^\infty \Lambda_i^*(\lambda)(\lambda^2 - 1)^c \lambda^d \Lambda_j(\lambda) d\lambda \quad (15)$$

The normalization constants can be calculated from:

$$N_i^{-2} = \left(\frac{R}{2}\right)^3 [\Omega_{i,i}(0, 0, 0, 2) - \Omega_{i,i}(0, 2, 0, 0)] \times \int \Phi_i^*(\phi) \Phi_i(\phi) d\phi \quad (16)$$

$$N_j^{-2} = \left(\frac{R}{2}\right)^3 [\Omega_{j,j}(0, 0, 0, 2) - \Omega_{j,j}(0, 2, 0, 0)] \times \int \Phi_j^*(\phi) \Phi_j(\phi) d\phi \quad (17)$$

After calculating the values of $Q_{i,j}(\mathbf{r})$ for each components x, y and z, we obtain D_{ij} as follows (Herman & Wallis 1956):

$$|D_{ij}|^2 = |eQ_{i,j}(x)|^2 + |eQ_{i,j}(y)|^2 + |eQ_{i,j}(z)|^2 \quad (18)$$

We compute the values of the electric dipole moments, equation (18), for all transitions of the Lyman and Balmer series for the H_2^+ molecular ion for internuclear separations up to 300 a.u. .

Table 1 shows values of the electric dipole moments of this work compared with those of Ramaker & Peek (1973) for some transitions, demonstrating that our work presents a higher precision and greater coverage of the internuclear distance.

For equations (6) and (8) to be solutions of the appropriate electronic functions Ψ_i , the summations must be allowed to go to infinity. However, we achieve convergence of the series for $s = 31$ and $t = 10$.

The data of the potential and electric dipole moments are plotted in subsequent sections for the Lyman series (Ly α to Ly δ) and Balmer- α . Electric dipole moments are plotted for Balmer- α and Balmer- β .

3 PROFILES AND SATELLITES

Currently there are different approaches to the calculation of the line profiles, namely, quasi-static, quantum-mechanical and unified theory.

In the quasi-static approximation, the expression of the cross-section may be written as (Margenau & Lewis 1959; Allard & Kielkopf 1982; Rohrmann et al. 2011)

$$\sigma_{ij}(\nu) = \frac{16}{3} \pi^3 n_p \alpha \left\{ \frac{h\nu}{|dV_{ij}/dR|} \right\} D_{ij} R^2 e^{(4\pi n_p R^3/3)} e^{-\beta E_i(R)}, \quad (19)$$

where $\beta = \frac{1}{kT}$, k is the Boltzmann constant, and T is the gas temperature. n_p is the mean density of perturbers in the gas, V_{ij} the potential energy difference associated with a transition with an energy $h\nu = V_{ij} \equiv V_j(R) - V_i(R)$ at internuclear separation R , $D_{ij}(R)$ is the dipole moment, and $E_i(R)$ corresponds to the change in energy (with respect to $R = \infty$) in the state i of the H_2^+ . When there is an extreme in the curve corresponding to the difference in the potential

Table 1. Table of comparison between the data of Ramaker & Peek (1973)[†] and this work[‡] of the electric dipole moments for Lyman- α of the H_2^+ in atomic units.

$R(a_0)$	Transition	$Q_{\alpha,\beta}(R)^\dagger$	$Q_{\alpha,\beta}(R)^\ddagger$
1.0	$2p\pi_u-1s\sigma_g$	0.5494	0.5493774
11.0	$2p\pi_u-1s\sigma_g$	0.7169	0.7168555
60.0	$2p\pi_u-1s\sigma_g$	0.7450	0.7449931
1.0	$3p\sigma_u-1s\sigma_g$	0.1651	0.1651107
11.0	$3p\sigma_u-1s\sigma_g$	0.4859	0.4858565
80.0	$3p\sigma_u-1s\sigma_g$	0.5207	0.5207119
1.0	$4f\sigma_u-1s\sigma_g$	0.001055	0.0010541
11.0	$4f\sigma_u-1s\sigma_g$	0.6609	0.6608712
80.0	$4f\sigma_u-1s\sigma_g$	0.5326	0.5325508
1.0	$2s\sigma_g-2p\sigma_u$	1.241	1.2406089
11.0	$2s\sigma_g-2p\sigma_u$	0.4844	0.4844248
80.0	$2s\sigma_g-2p\sigma_u$	0.5207	0.5207119
1.0	$3d\sigma_g-2p\sigma_u$	1.010	1.0104411
11.0	$3d\sigma_g-2p\sigma_u$	0.6349	0.6349347
80.0	$3d\sigma_g-2p\sigma_u$	0.5326	0.5325508
1.0	$3d\pi_g-2p\sigma_u$	0.8584	0.8584398
11.0	$3d\pi_g-2p\sigma_u$	0.7935	0.7935359
60.0	$3d\pi_g-2p\sigma_u$	0.7450	0.7449931

energies between the upper and lower states, $\frac{dV_{ij}}{dR}$ is zero. Therefore, if the derivative is zero, there is a divergence, called a satellite line.

In the quantum-mechanical approach, the cross section for the spontaneous plus stimulated association process is given by (Zygelman & Dalgarno 1990)

$$\sigma(E) = \sum_{N'} \sum_{v''} \frac{64}{3} \frac{\pi^5}{c^3} \frac{\nu^3}{\kappa^2} \frac{1}{1 - \exp(-h\nu/kT)} \times p[N' M_{v'', N'-1; \kappa, N'}^2 + (N' + 1) M_{v'', N'+1; \kappa, N'}^2] \quad (20)$$

where E is the relative collision energy, κ is the wave number of relative motion, p is the probability of approach in the initial electronic state, N' is the initial rotational quantum number, v'' is the final vibrational quantum number, and M is the electric dipole matrix element connecting the initial continuum and final rotational-vibrational states of the ground electronic state.

The unified theory has been developed in Allard et al. (1999), and a detailed discussion is presented there. The fundamental expression of the normalized spectrum line $F_\nu(\Delta\nu)$ is computed from the Fourier transform (Allard et al. 2009)

$$F_\nu(\Delta\nu) = \frac{1}{\pi} \text{Re} \int_0^{+\infty} \Phi(s) e^{-i\Delta\nu s} ds. \quad (21)$$

Figure 1 shows the comparison of the line profile of Ly α of the three approaches mentioned above. The solid line shows the approach from the unified theory, which has a resolution determined by Fourier transform (equation 21), while the quantum-mechanical approaches (dashed line) and quasi-static (solid line) values provide similar but distinct profiles due to the calculation of the derivative by the numerical difference in the quasi-static and by the series expansion in quantum-mechanics. The three profiles are similar; however, the quasi-static approach better represents the correct

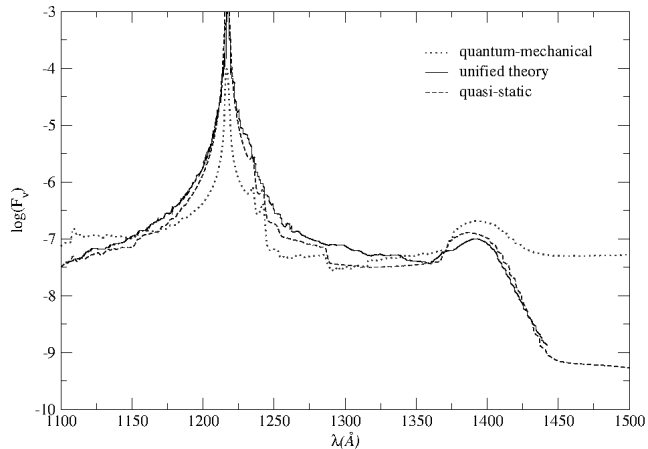


Figure 1. Comparison of the line profile of Lyman- α normalized between the three approaches, quasi-static (dashed line), quantum-mechanical (dotted line) and unified theory (solid line) adapted from Allard et al. (1999).

global shape of the line wings and position of the satellites, in comparison with previously published data (Allard et al. 1999). As the main aim of our work are: the calculations of the electric dipole moments, the potentials of H_2^+ ion, the calculations of the global shape of line profiles and the location of the satellites, we use the quasi-static approach to calculate the line profiles. Unfortunately, the quasi-static approach does not provide an appropriate shape of the center of the lines, thus there is a need for better modeling of the center lines of each transition.

Our interest is to find the correct position of the satellites in the wings of the line profile and their general form (i.e., the divergences in the profile) and bring these results to the attention of astrophysicists. If they are observable, they will be specific for protons (although other ions may give qualitatively similar effects).

The method we used to obtain the profiles following Rohrmann et al. (2011). For lines profile of the Lyman and Balmer series in a quasi-static approach, we identified each pair of levels (i, j) of the quasi-molecule $H - H^+$ that contributes to the formation of a given line. Only transitions between states u (ungerade) and g (gerade) are allowed, i.e., with opposite parity and taking $|m - m'| = 0$ or 1 as the allowed dipole. The second step is to calculate the effective cross section $\sigma_{ij}(\nu)$, equation (19) using the potentials and dipole moments for the transitions already identified. For the calculation of $\sigma_{ij}(\nu)$ we need to analyze the frequencies ν that arise from the difference in energy between these levels $h\nu = V_j - V_i$. However, we must take into account that different internuclear distances can produce the same frequency. The effective cross section is the sum of each of these contributions.

The line profile is the sum of the effective cross sections $\sigma_{ij}(\nu)$ multiplied by the statistical weights of each of the respective transitions. The calculated profile was convolved with a Maxwellian distribution of velocities to take into account the thermal Doppler broadening.

The line profiles and satellite lines of Lyman and Balmer series shown in this paper are for single densities of 10^{16} to 10^{18} cm^{-3} , typical of the atmosphere of white dwarf stars

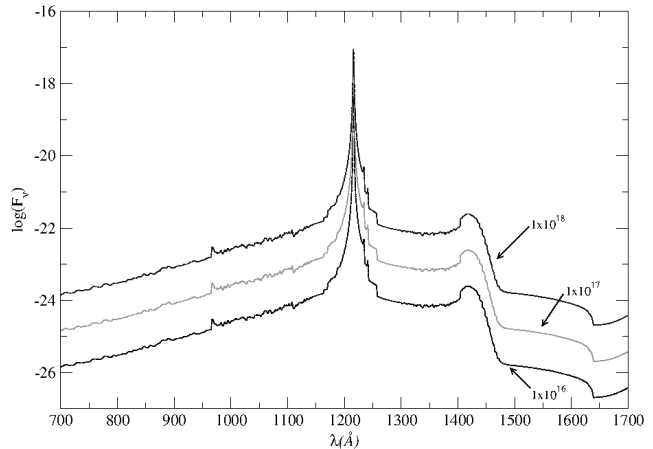


Figure 2. Lyman- α profile with density of H^+ perturbors ($T=4000 \text{ K}$), $n_H^+ = 10^{16}$, $n_H^+ = 10^{17}$ and $n_H^+ = 10^{18} \text{ cm}^{-3}$ (from bottom to top).

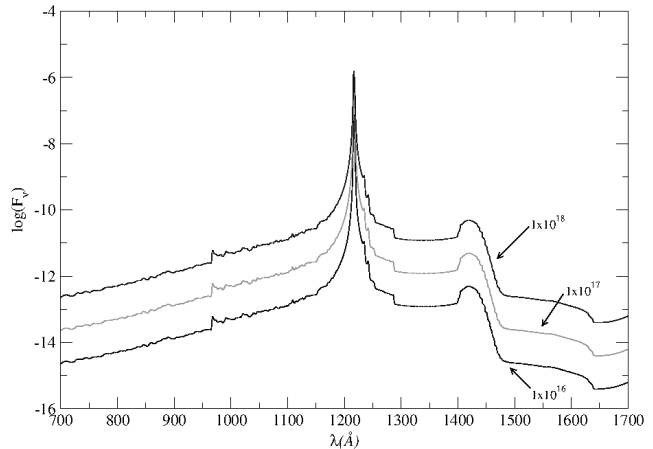


Figure 3. Lyman- α profile with density of H^+ perturbors ($T=12000 \text{ K}$), $n_H^+ = 10^{16}$, $n_H^+ = 10^{17}$ and $n_H^+ = 10^{18} \text{ cm}^{-3}$ (from bottom to top).

and that can be produced in z-pinch laboratories. We remind the reader that the real profile must include the electrons Stark broadening, which do not have satellites.

3.1 Lyman series

3.1.1 Lyman- α

The Lyman- α total profile depends on 6 individual transitions. The line profile calculations shown in Figures 2 and 3 have been done for temperatures of 4000 K and 12000 K, at proton densities of 10^{16} , 10^{17} and 10^{18} cm^{-3} .

Figure 4 shows the potential energy for the transitions that contribute to the profile of Lyman- α and Figure 5 shows the electronic transition dipole moments for Lyman- α due to H perturbed by collisions with protons.

Table 2 lists the wavelengths of the satellite lines with the upper and lower state identifications and the distance of the atom-ion pair at which the potential extreme occurs. Several of these features can be identified in the total Lyman- α profile of Figures 2 and 3.

Table 2. Allowed transitions and satellites due to H - H⁺ collisions of Lyman- α to the distance R(\AA) of the atom-ion pair at which the potential extreme occurs.

Label	Upper level	Lower level	$\Delta\nu_{H_2^+}$ (cm^{-1})	$\lambda_{H_2^+}$ (\AA)	R (\AA)
1	$2p\pi_u$	$1s\sigma_g$	-1628.54	1240.56	4.72
2	$3p\sigma_u$	$1s\sigma_g$	-	-	-
3	$4f\sigma_u$	$1s\sigma_g$	-1172.40	1233.58	11.07
4	$2s\sigma_g$	$2p\sigma_u$	8139.91	1106.47	2.65
5	$3d\sigma_g$	$2p\sigma_u$	-11055.90	1404.87	4.56
			16001.33	1017.93	1.39
6	$3d\pi_g$	$2p\sigma_u$	21384.28	965.05	1.67

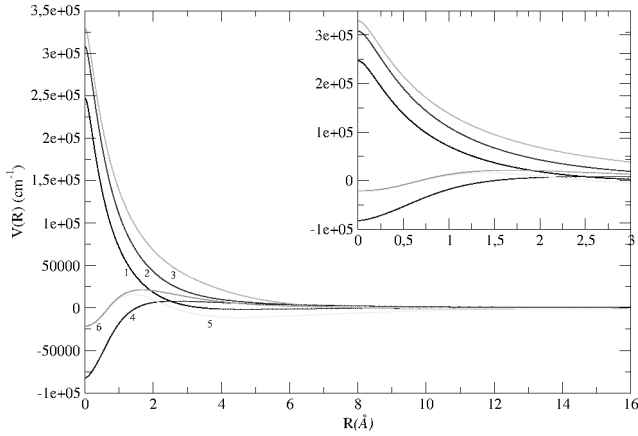


Figure 4. Transitions difference potential as a function of inter-atomic distance of the H₂⁺ of Lyman- α .

We list in Table 2 the satellite around $\lambda = 1400 \text{ \AA}$, observed by Koester et al. (1985) and Nelan & Wegner (1985), who proposed the lines are caused by quasi-molecular absorption of the H₂⁺ molecule.

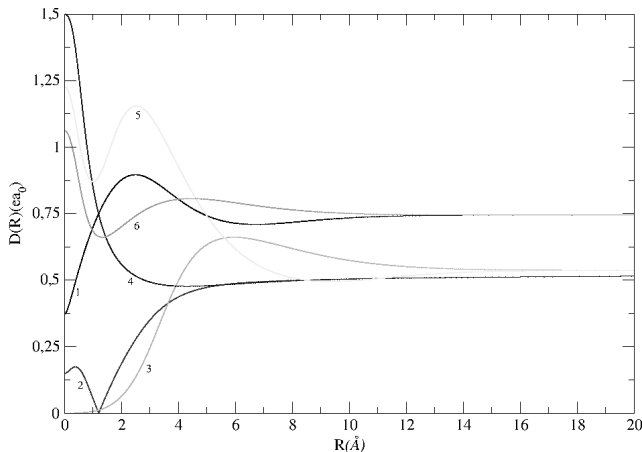


Figure 5. Electronic transition dipole moments of Lyman- α due to H perturbed by collisions with protons. The $D(R)$ is given here in atomic units.

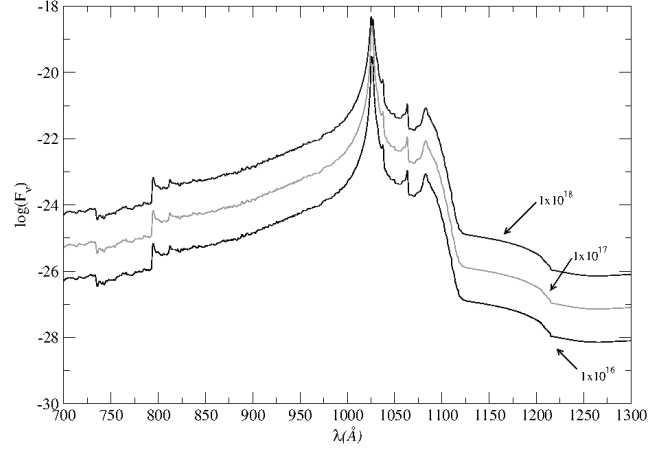


Figure 6. Lyman- β profile for T = 4000 K and density of H⁺ perturbors of $n_H^+ = 10^{16}$, $n_H^+ = 10^{17}$ and $n_H^+ = 10^{18} \text{ cm}^{-3}$ (from bottom to top).

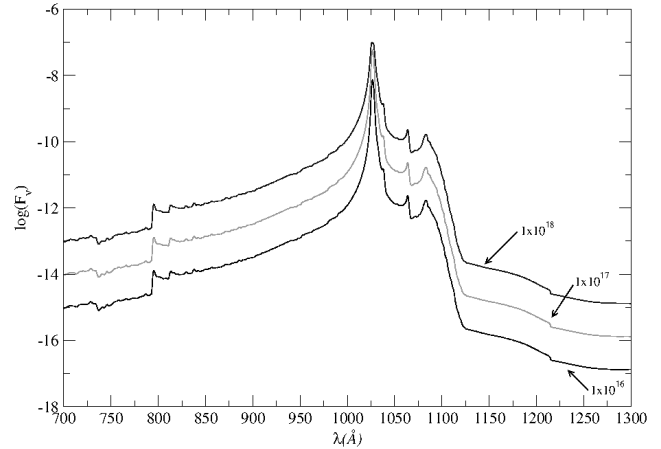


Figure 7. Lyman- β profile for T = 12000 K, and density of H⁺ perturbors of $n_H^+ = 10^{16}$, $n_H^+ = 10^{17}$ and $n_H^+ = 10^{18} \text{ cm}^{-3}$ (from bottom to top).

3.1.2 Lyman- β

The profile of Lyman- β depends on 10 transitions. Table 3 lists all the wavelengths of these transitions and the possible lines satellites. Satellites of Lyman- β were observed in the spectra of the DA white dwarf Wolf 1346 with the Hopkins Ultraviolet Telescope (HUT) (Koester et al. 1996). Koester et al. (1998) observed satellites absorption features at $\lambda = 1060 \text{ \AA}$ and $\lambda = 1080 \text{ \AA}$ in the spectra of 4 other targets obtained with the Orbiting and Retrievable Far and Extreme Ultraviolet Spectrometer (ORFEUS). These satellites are due to the contributions of the transitions $4f\pi_u-1s\sigma_g$ and $5g\sigma_g-2p\sigma_u$ of the profile of Lyman- β , according to the profiles of calculated by Allard et al. (1998a).

The Ly β line profiles shown in Figures 6 and 7 are for temperatures of 4000 K and 12000 K, and densities of protons 10^{16} , 10^{17} and 10^{18} cm^{-3} . Figure 8 shows all the differences of the potential energy of the transitions that contribute to the Lyman- β line profile. In Figure 9, we plot the dipole $D(R)$ for transitions of the Lyman- β due to H perturbed by collisions with protons.

Table 3. Allowed transitions and satellites due to H - H⁺ collisions of Lyman- β to the distance R(\AA) of the atom-ion pair at which the potential extreme occurs.

Label	Upper level	Lower level	$\Delta\nu_{H_2^+}$ (cm^{-1})	$\lambda_{H_2^+}$ (\AA)	R (\AA)
1	3p π_u	1s σ_g	-	-	-
2	4p σ_u	1s σ_g	-	-	-
3	4f π_u	1s σ_g	-3361.25	1062.64	9.85
4	5f σ_u	1s σ_g	-	-	-
5	6h σ_u	1s σ_g	-1037.33	1037.03	21.45
6	3s σ_g	2p σ_u	22200.04	835.65	1.96
7	4d σ_g	2p σ_u	-633.34	1032.71	9.46
			25868.59	810.80	1.55
8	4d π_g	2p σ_u	28666.11	792.82	1.70
9	5g σ_g	2p σ_u	-4899.9272	1080.31	12.65
			38880.59	733.42	1.69
10	5g π_g	2p σ_u	-516.61	1031.46	18.89
			38914.86	733.24	1.69

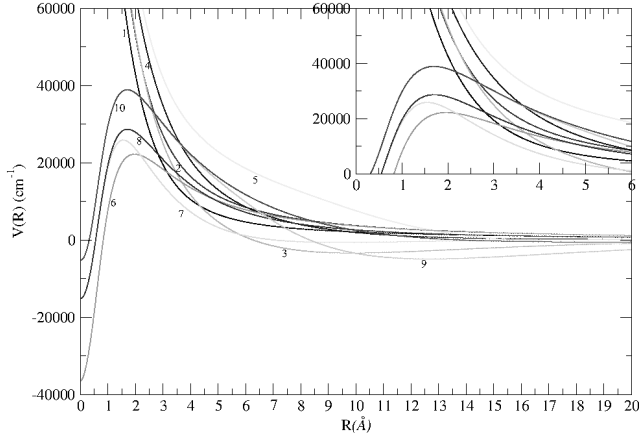


Figure 8. Transition potential energies as a function of inter-atomic distance of the H₂⁺ of Lyman- β .

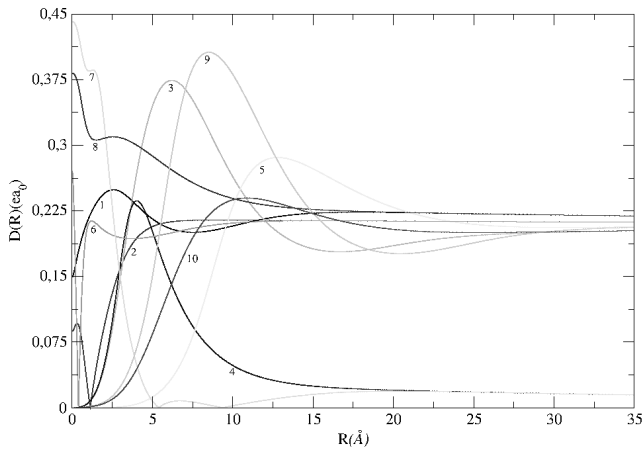


Figure 9. Electronic transition dipole moments of Lyman- β due to H perturbed by collisions with protons. The $D(R)$ is given here in atomic units.

Table 4. Allowed transitions and satellites due to H - H⁺ collisions of Lyman- γ to the distance R(\AA) of the atom-ion pair at which the potential extreme occurs.

Label	Upper level	Lower level	$\Delta\nu_{H_2^+}$ (cm^{-1})	$\lambda_{H_2^+}$ (\AA)	R (\AA)
1	4p π_u	1s σ_g	-	-	-
2	5p σ_u	1s σ_g	-	-	-
3	5f π_u	1s σ_g	-192.78	974.62	16.65
4	6f σ_u	1s σ_g	-	-	-
5	6h π_u	1s σ_g	-2188.78	993.96	20.69
6	7h σ_u	1s σ_g	-230.90	974.98	29.66
7	8j σ_u	1s σ_g	-784.17	980.27	36.06
8	4s σ_g	2p σ_u	30153.49	752.16	1.82
9	5d σ_g	2p σ_u	32004.30	741.83	1.62
10	5d π_g	2p σ_u	33520.98	733.58	1.70
11	6g σ_g	2p σ_u	-1395.38	986.18	17.79
			39005.56	705.21	1.69
12	6g π_g	2p σ_u	39025.78	705.11	1.69
13	7i σ_g	2p σ_u	-2627.07	998.31	25.06
			42340.74	689.00	1.70
14	7i π_g	2p σ_u	-565.52	978.18	31.65
			42342.54	688.99	1.70

3.1.3 Lyman- γ

There are 14 allowed transitions due to collisions of H - H⁺ and the satellites predicted to occur are listed in Table 4. The satellite absorption features at $\lambda = 995 \text{ \AA}$ was observed in a HUT spectrum and later in spectra recorded by ORFEUS. This Lyman- γ satellite was also visible in the spectra of the white dwarf *CD - 38°10980* (Wolff et al. 2001) and Sirius B (Holberg et al. 2003). Allard et al. (2004) calculated the profiles of Lyman- γ line based on accurate *ab initio* potentials to explain the observation of this feature.

The line profile calculations shown in Figure 10 and Figure 11 have been evaluated at a temperature of 4000 K and 12000 K for different densities of protons 10^{16} , 10^{17} and 10^{18} cm^{-3} .

Figure 12 shows all the potential energy differences for the transitions that contribute to the Lyman- γ line profile and Figure 13 plots the electronic transition dipole moments for Lyman- γ due to H perturbed by collisions with protons.

3.1.4 Lyman- δ

There are 18 allowed transitions due to collisions of H and H⁺, and the satellites predicted to occur are listed in Table 5.

Figures 14 and 15 show the line profiles as a function of temperature and density of perturbors.

Figure 16 shows all the potential energy differences for the of the transitions that contribute to the line profile of Lyman- δ . Figure 17 shows the electronic transition dipole moments for Lyman- δ of the H₂⁺ and Figure 18 shows the total line profiles of Ly α , Ly β , Ly γ and Ly δ perturbed by protons for a single T= 12000 K and $n_H^+ = 10^{17} \text{ cm}^{-3}$. This figure is similar to Figure 3 obtained by Hébrard et al. (2011), showing that our calculations and approximations are consistent with data already published.

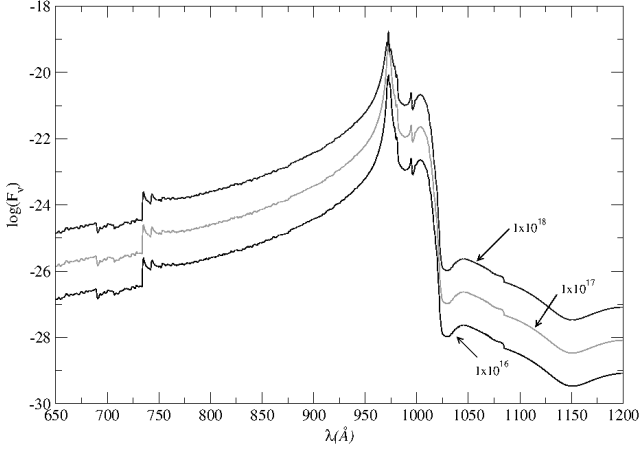


Figure 10. Variation of the Lyman- γ profile with density of H^+ perturbors ($T = 4000$ K), $n_H^+ = 10^{16}$, $n_H^+ = 10^{17}$ and $n_H^+ = 10^{18}$ cm^{-3} (from bottom to top).

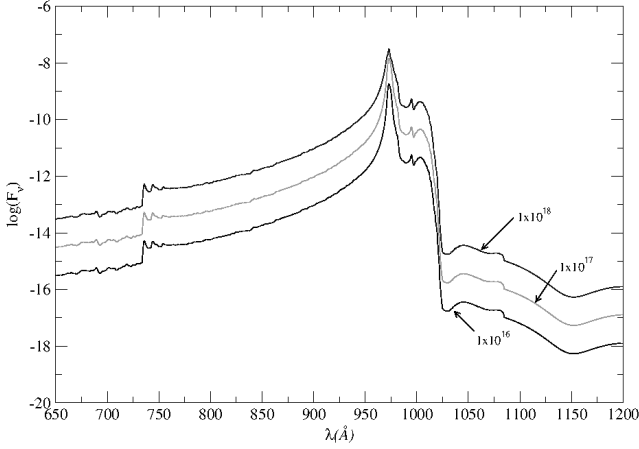


Figure 11. Variation of the Lyman- γ profile with density of H^+ perturbors ($T = 12000$ K), $n_H^+ = 10^{16}$, $n_H^+ = 10^{17}$ and $n_H^+ = 10^{18}$ cm^{-3} (from bottom to top).

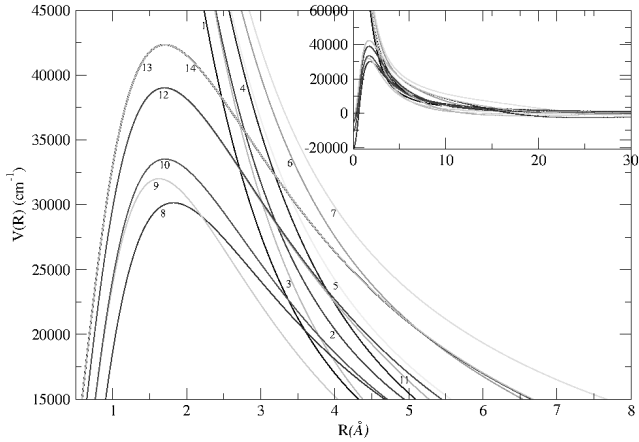


Figure 12. Transition potential energy differences as a function of interatomic distance of the H_2^+ of Lyman- γ .

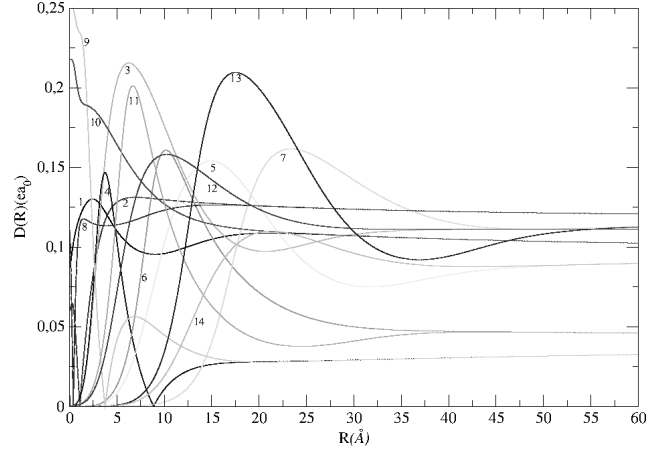


Figure 13. Electronic transition dipole moments of Lyman- γ due to H perturbed by collisions with protons. The $D(R)$ is given here in atomic units.

Table 5. Allowed transitions and satellites due to H - H^+ collisions of Lyman- δ to the distance $R(\text{\AA})$ of the atom-ion pair at which the potential extreme occurs.

Label	Upper level	Lower level	$\Delta\nu_{H_2^+}$ (cm^{-1})	$\lambda_{H_2^+}$ (\AA)	R (\AA)
1	$5p\pi_u$	$1s\sigma_g$	-	-	-
2	$6p\sigma_u$	$1s\sigma_g$	-	-	-
3	$6f\pi_u$	$1s\sigma_g$	-	-	-
4	$7f\sigma_u$	$1s\sigma_g$	-	-	-
5	$7h\pi_u$	$1s\sigma_g$	-679.23	956.16	27.56
6	$8h\sigma_u$	$1s\sigma_g$	-	-	-
7	$8j\pi_u$	$1s\sigma_g$	-1413.57	962.93	36.17
8	$9j\sigma_u$	$1s\sigma_g$	-312.56	952.82	44.76
9	$10l\sigma_u$	$1s\sigma_g$	-582.87	955.28	54.98
10	$5s\sigma_g$	$2p\sigma_u$	-	-	-
11	$6d\sigma_g$	$2p\sigma_u$	-	-	-
12	$6d\pi_g$	$2p\sigma_u$	-	-	-
13	$7g\sigma_g$	$2p\sigma_u$	-76.95	950.69	26.02
14	$7g\pi_g$	$2p\sigma_u$	-	-	-
15	$8i\sigma_g$	$2p\sigma_u$	-1119.44	960.21	31.54
16	$8i\pi_g$	$2p\sigma_u$	-99.84	950.90	42.38
17	$9k\sigma_g$	$2p\sigma_u$	-1589.40	964.56	41.91
18	$9k\pi_g$	$2p\sigma_u$	-475.45	954.31	49.00

3.2 Balmer series

The Balmer lines have transitions that must obey the same golden rules as the Lyman series transitions.

3.2.1 Balmer- α

The total profile of Balmer- α depends on the 32 individual transitions. The line profile calculations shown in Figure 23 have been calculated at a single temperature of 12000 K and protons density of 10^{17} cm^{-3} .

Table 6 lists only the transitions that generate possible satellite lines on the wings of the Balmer line profiles. In Figure 19 we plot the transition dipole moments for the satellites listed in Table 6. In laboratory observations, measurements of the spectrum of a laser-produced plasma confirm that the $\lambda = 8650 \text{ \AA}$ satellite exists in the $H\alpha$ red

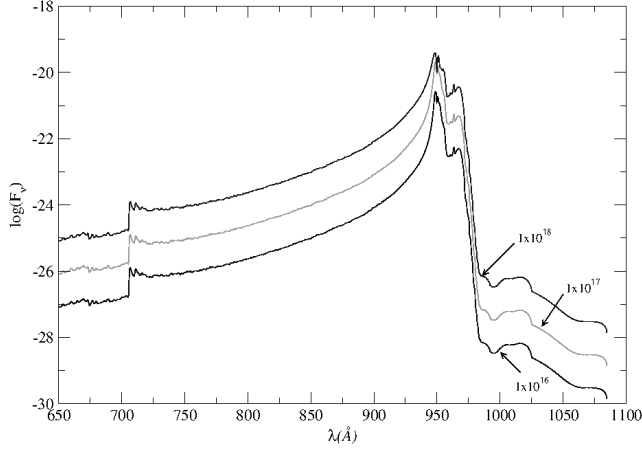


Figure 14. Lyman- δ profile for density of H^+ perturbors ($T=4000$ K), $n_H^+ = 10^{16}$, $n_H^+ = 10^{17}$ and $n_H^+ = 10^{18} \text{ cm}^{-3}$ (from bottom to top).

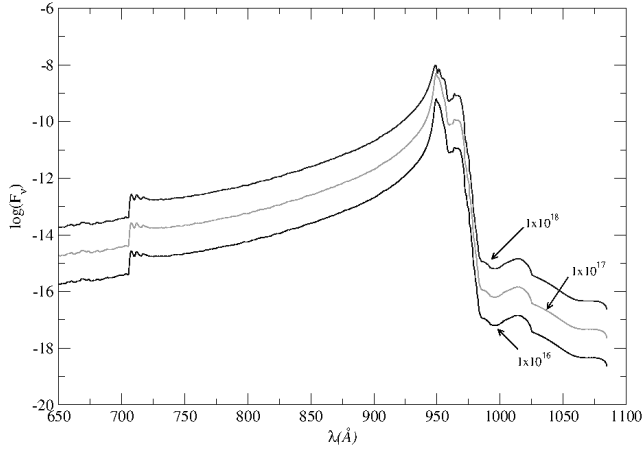


Figure 15. Lyman- δ profile for density of H^+ perturbors ($T=12000$ K), $n_H^+ = 10^{16}$, $n_H^+ = 10^{17}$ and $n_H^+ = 10^{18} \text{ cm}^{-3}$ (from bottom to top).

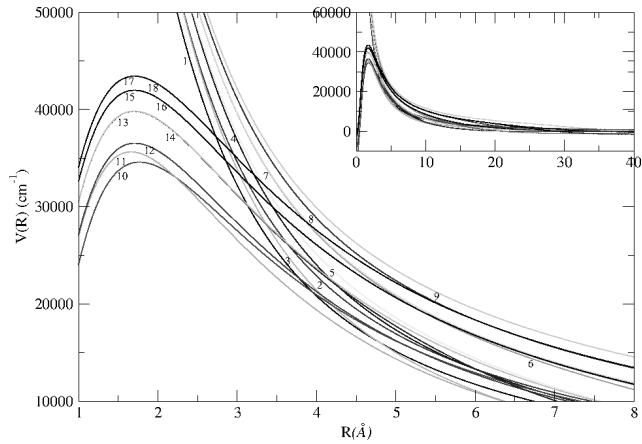


Figure 16. Potential energy differences for the allowed transitions, as a function of interatomic distance of the H_2^+ of Lyman- δ .

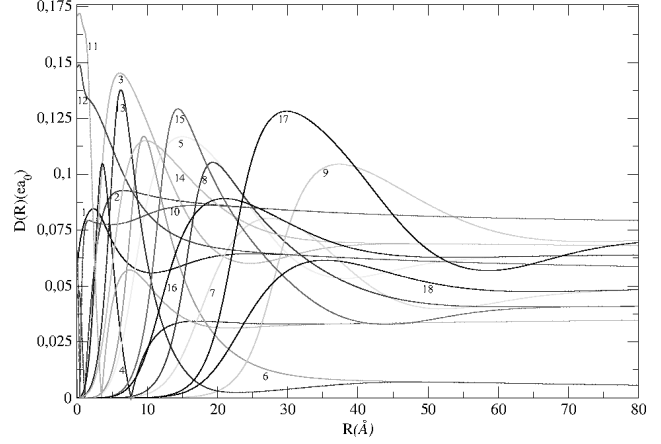


Figure 17. Electronic transition dipole moments of Lyman- δ due to H perturbed by collisions with protons. The $D(R)$ is given here in atomic units.

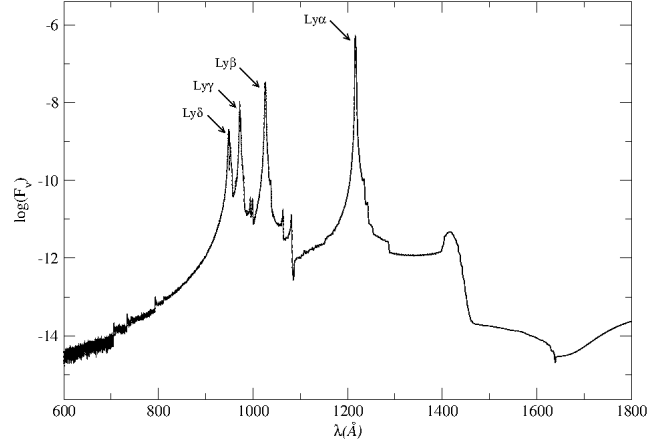


Figure 18. Total profile of Lyman- α , Lyman- β , Lyman- γ and Lyman- δ perturbed by protons ($n_H^+ = 10^{17} \text{ cm}^{-3}$) at a temperature $T=12000$ K.

wing (Kielkopf et al. 2002) due the transitions $5g\sigma_g-4f\sigma_u$ and $4f\pi_u-3d\pi_g$.

Figure 20 shows the comparison between the VCS (Vidal et al. 1973) profile calculated by Koester (private communication) for $T=12000$ K and n_H^+ density 10^{16} cm^{-3} , with the profile of H_2^+ calculated for the same temperature and density. It is observed that at high energies both profiles coincide asymptotically, while, due to possible formation of low-energy molecules, discrepancies arise between the profiles.

3.2.2 Balmer- β

The total profile of Balmer- β depends on the 46 individual transitions. Figure 21 shows the profile of $H\beta$ calculated for protons density of $9.324 \times 10^{16} \text{ cm}^{-3}$ and $1.554 \times 10^{18} \text{ cm}^{-3}$ with $T=13526$ K. We can see the center of the line is split and asymmetric.

Table 7 lists the lines satellites due to the $H\beta$ and Figure 22 plots the respective transitions listed in the same table. The line profile calculations shown in Figure 23 is for temperature of 12000 K and protons density of 10^{17} cm^{-3} .

Table 6. Satellites due to H - H⁺ collisions of Balmer- α to the distance R(\AA) of the atom-ion pair at which the potential extreme occurs.

Label	Upper level	Lower level	$\Delta\nu_{H_2^+}$ (cm^{-1})	$\lambda_{H_2^+}$ (\AA)	R (\AA)
1	5g σ_g	4f σ_u	-3844.18	8783.59	13.10
			4956.58	4954.01	5.60
2	5g σ_g	2p π_u	-4996.57	9772.81	12.66
3	6h σ_u	3d σ_g	40925.21	1780.80	3.17
			-702.54	6883.97	23.03
4	4f π_u	3d σ_g	-1271.27	7164.46	13.13
			23797.73	2562.34	3.06
5	4d σ_g	3p σ_u	-3214.16	8323.01	6.47
			12145.77	3652.99	1.01
6	4f π_u	3d π_g	-3658.85	8642.89	9.33
			7163.74	4465.72	1.69
7	4f π_u	2s σ_g	-5245.35	10016.33	8.69
			37537.98	1895.12	1.00
8	5f σ_u	2s σ_g	-424.84	6754.83	15.47
9	6h σ_u	2s σ_g	-1500.75	7284.22	20.33
10	4d σ_g	2p π_u	-634.82	6852.02	10.20
11	5g π_g	2p π_u	-601.70	6836.51	18.74
12	5g σ_g	3p σ_u	-6042.60	10885.60	12.08
			23287.20	2596.30	1.18
13	5g π_g	3p σ_u	-1130.91	7093.14	16.58
			23303.15	2595.23	1.18
14	6h σ_u	3d π_g	-1117.22	7086.25	21.38
			23163.48	2604.67	2.10

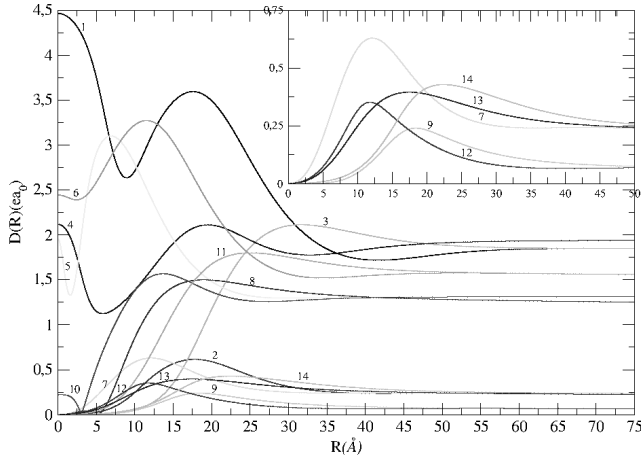


Figure 19. Transition dipole moments for the satellites of Balmer- α due to H perturbed by collision with protons. The transitions plotted here are listed in Table 6. The $D(R)$ is given here in atomic units.

3.2.3 Balmer- γ

The total profile of Balmer- γ depends on the 60 individual transitions. The line profile shown in Figure 23 is for a temperature of 12 000 K and proton density 10^{17} cm^{-3} .

3.2.4 Balmer- δ

The total profile of Balmer- δ depends on the 74 individual transitions. The line profile calculations of Figure 23 have

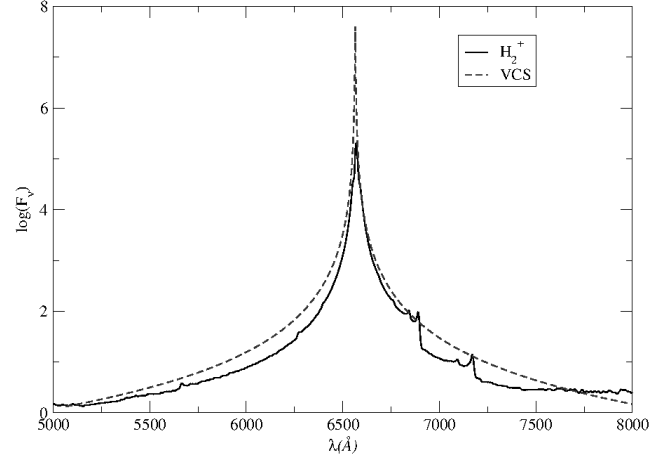


Figure 20. Comparison between the profile of Balmer- α of H₂⁺ with the profile VCS - electron Stark broadening, for T= 12 000 K and density 10^{16} cm^{-3} .

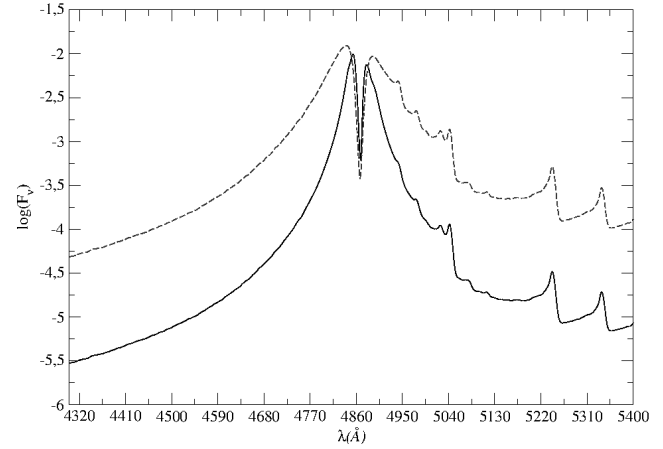


Figure 21. Solid line is the Balmer- β profile with density $n_H^+ = 9.324 \times 10^{16} \text{ cm}^{-3}$ of the perturbors and $T = 13\,526 \text{ K}$. Dashed line is the Balmer- β profile with density $n_H^+ = 1.554 \times 10^{18} \text{ cm}^{-3}$ of the perturbors and $T = 13\,526 \text{ K}$. The line profile can be used for diagnostic of the physical conditions of a laboratory measurements.

been done at a temperature of 12 000 K for the protons density 10^{17} cm^{-3} .

3.2.5 Balmer- ϵ

The total profile of Balmer- ϵ depends on the 88 individual transitions. The line profile calculations of Figure 23 have been done at a temperature of 12 000 K for the protons density 10^{17} cm^{-3} .

3.2.6 Balmer-8

The total profile of Balmer-8 depends on the 102 individual transitions. The line profile calculations of Figure 23 have been done at a temperature of 12 000 K for the protons density 10^{17} cm^{-3} .

Table 7. Satellites due to H - H⁺ collisions of Balmer- β to the distance R(\AA) of the atom-ion pair at which the potential extreme occurs.

Label	Upper level	Lower level	$\Delta\nu_{H_2^+}$ (cm^{-1})	$\lambda_{H_2^+}$ (\AA)	R (\AA)
1	5f π_u	2s σ_g	-992.00	5110.59	13.83
2	6h π_u	2s σ_g	-2674.11	5591.24	19.90
3	5g δ_g	2p π_u	-1466.46	5237.59	16.80
4	6g σ_g	2p π_u	-1483.16	5242.17	17.74
5	6g σ_g	3p σ_u	-2040.74	5400.01	16.50
			23365.48	2276.62	1.19
6	7i σ_g	3p σ_u	-2977.17	5687.62	24.59
			26648.74	2118.28	1.19
7	7i π_g	3p σ_u	-816.65	5065.20	29.99
			26649.62	2118.24	1.19
8	6h π_u	3d σ_g	-1811.98	5334.12	21.66
			35621.24	1779.97	3.17
9	8j σ_u	3d σ_g	-381.85	4956.05	29.99
			41130.19	1621.02	3.19
10	5f π_u	3d π_g	-285.48	4932.49	16.46
			12088.84	3062.96	1.91
11	6h π_u	3d π_g	-2269.96	5467.69	20.64
			17843.96	2603.95	2.11
12	6h δ_u	3d π_g	-308.92	4938.20	28.53
			17875.84	2601.79	2.13
13	7h σ_u	3d π_g	-302.86	4936.72	29.57
			21106.24	2400.06	2.12
14	8j σ_u	3d π_g	-853.70	5074.72	36.03
			23255.19	2282.35	2.15
15	5d σ_g	4f σ_u	-11612.48	11177.27	1.95
			3925.46	4084.18	8.17
16	6g σ_g	4f σ_u	-878.51	5081.12	20.00
			6602.41	3681.66	6.08
17	7i π_g	4f σ_u	-405.68	4961.91	29.99
			12418.51	3032.34	6.81

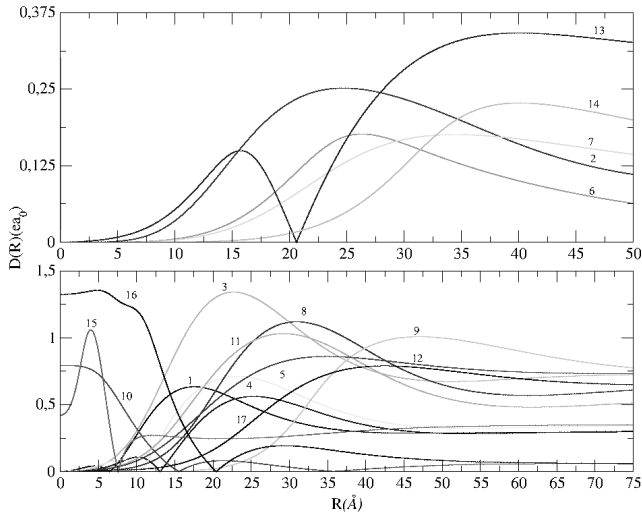


Figure 22. Electronic Transition dipole moments for the satellites of Balmer- β due to H perturbed by collision with protons. The transitions plotted here are listed in Table 7. The $D(R)$ is given here in atomic units.

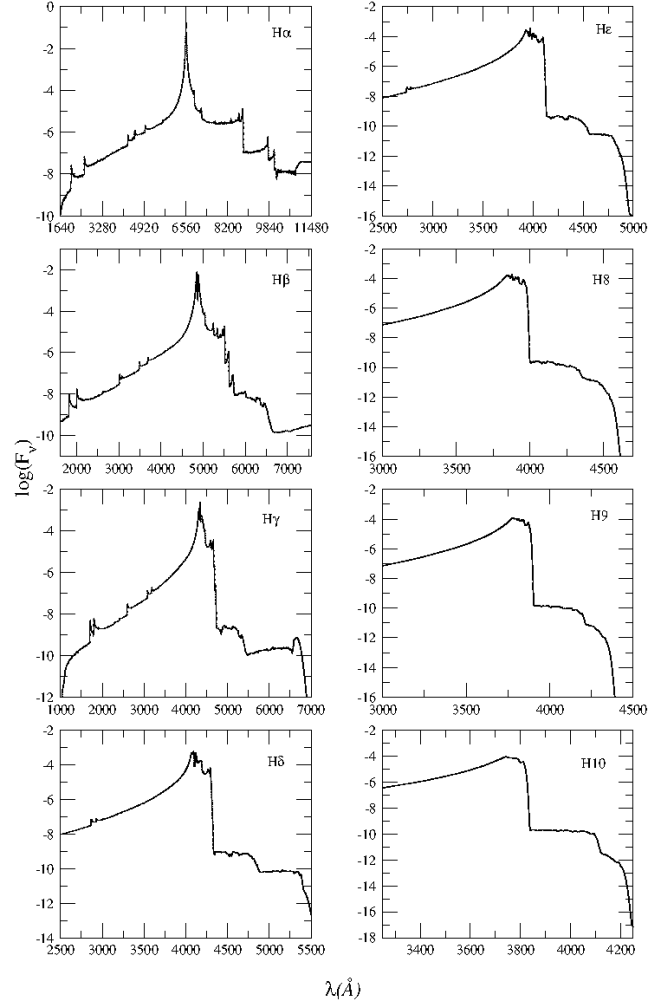


Figure 23. Profiles of the Balmer series (H α , H β , H γ , H δ , H ϵ , H8, H9, and H10) for ion density $n_H^+ = 10^{17} \text{ cm}^{-3}$ and T= 12 000 K.

3.2.7 Balmer-9

The total profile of Balmer-9 depends on the 116 individual transitions. The line profile calculations of Figure 23 have been done at a temperature of 12 000 K for the protons density 10^{17} cm^{-3} .

3.2.8 Balmer-10

The total profile of Balmer-10 depends on the 130 individual transitions. The line profile calculations of Figure 23 have been done at a temperature of 12 000 K for the protons density 10^{17} cm^{-3} .

4 DISCUSSION AND CONCLUSION

Satisfactory theory and data for the line profiles do exist due to the electron Stark broadening of neutral hydrogen (Lemke 1997; Vidal et al. 1973), and for 21 optical lines of neutral helium (Barnard et al. 1969; Beauchamp et al. 1997). The first three Lyman lines of H broadened by ionized and neutral perturbers, including a number of satellite features, are well described by the work of Nicole Allard

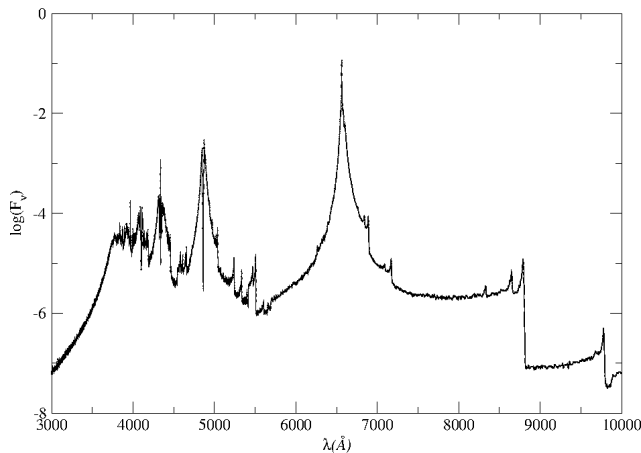


Figure 24. Total profile of the Balmer for $T= 12000$ K and $n_H^+ = 10^{17} \text{ cm}^{-3}$.

and collaborators (e.g. Allard et al. 2009, and papers cited therein), and the atomic data are obtained from a number of atomic databases, predominantly the line lists from Kurucz and collaborators (Kurucz & Bell 1995), and the Vienna Atomic Line Database (VALD) (Kupka et al. 1999, 2000; Ryabchikova et al. 1997; Piskunov et al. 1995). For all other cases the situation is much less satisfactory, so there is a need for theories and data to explain the line profiles and satellite lines.

We extended the potentials dipole and line profile calculations to $n=10$ for the collision of H on H^+ perturbers important at high densities, as observed in the atmosphere of white dwarf stars.

The laboratory observations of a laser-produced plasma confirm that satellites appear on Lyman- α due to collisions with neutral atoms and protons. This experimental confirmation of the theory supports the identification of these features in the Lyman- α spectra of white dwarf and λ Bootis stars. In high temperature plasmas such as laser-produced plasmas, dielectronic recombination process is very important. This process strongly affects the ion abundances and produces dielectronic satellite lines. The satellite lines appear near the resonance line through spontaneous radiative decay from the autoionizing states. Satellite line emissions from highly ionized ions are often used for plasma diagnostics which are important in various kinds of plasmas, e.g., Tokamak, inertial fusion, astrophysical and plasma sources, etc (Yamamoto et al. 2004). The comparison of the Lyman- α wing with line shape models is a tool for determining neutral and proton densities in a hydrogenic plasma. These experiments also confirm that the variation of the radiative dipole moment is an important factor in determining the far wing emission of Lyman- α . When $D(R)$ differs significantly from its asymptotic value at an R close to the region forming a satellite, the strength of the wing may be enhanced (or diminished) considerably.

In a collision-induced spectrum such as this one, the dipole moment may be more important than the potential in determining the shape of the satellite. These many-body perturbations alter the far line wing, adding multiple satellites and producing a strong continuum from the vacuum ultraviolet to the ultraviolet and visible.

The present calculations are done in an adiabatic approximation using a rectilinear trajectory. This should affect slightly the shape of the satellite, although no significant differences are expected.

The sum of the profiles calculated of Ly α , Ly β , Ly γ and Ly δ , are shown in Figure 18 and the sum of the profiles of Balmer series in Figure 24 to $T= 12000$ K and $n_H^+ = 10^{17} \text{ cm}^{-3}$. The ion collision profiles differs significantly from the electron Stark broadening, showing not only satellite lines but also significant wing values that affect the opacity.

The data is available in our web page at <http://astro.if.ufrgs.br/marcios>.

REFERENCES

- Allard N. F., Kielkopf J. F., Feautrier N., 1998a, *A&A*, 330, 782
- Allard N. F., Drira I., Gerbaldi M., Kielkopf J., Spielfiedel A., 1998b, *A&A*, 335, 1124
- Allard N. F., Royer A., Kielkopf J. F., Feautrier, N., 1999, *PhRvA*, 60, 1021
- Allard, N., & Kielkopf, J. 1982, *Reviews of Modern Physics*, 54, 1103
- Allard N. F., Kielkopf J. F., Hébrard G., Peek J. M., 2004, *European Physical Journal D*, 29, 7
- Allard N. F., Noselidze I., Kruk J. W., 2009, *A&A*, 506, 993
- Allard N. F., Kielkopf J., Drira I., Schmelcher P., 2000, *European Physical Journal D*, 12, 263
- Baber W. G., Hassé H. R., 1935, *Proceedings of the Cambridge Philosophical Society*, 31, 564
- Barnard A. J., Cooper J., Shamey, L. J., 1969, *A&A*, 1, 28
- Bates D. R., Poots G., 1953, *Proceedings of the Physical Society A*, 66, 784
- Beauchamp A., Wesemael F., Bergeron, P., 1997, *ApJS*, 108, 559
- Bergeron P., Saffer R. A., Liebert J., 1992, *ApJ*, 394, 228
- Bergeron P., Leggett S. K., 2002, *ApJ*, 580, 1070
- Bergeron P., Wesemael F., Fontaine G., 1991, *ApJ*, 367, 253
- Bergeron, P., Wesemael, F., Lamontagne, R., Fontaine, G., Saffer, R. A., & Allard, N. F. 1995, *ApJ*, 449, 258
- Burrau Ø., 1927, *Naturwissenschaften*, 15, 16
- Eisenstein D. J., Liebert J., Harris H. C., Kleinman S. J., Nitta A., Silvestri N., Anderson S. A. Barentine J. C., et al., 2006, *ApJS*, 167, 40
- Engelbrecht, A., & Koester, D. 2007, 15th European Workshop on White Dwarfs, 372, 289
- Falcon, R. E., Winget, D. E., Montgomery, M. H., & Williams, K. A. 2010, *Apj*, 712, 585
- Gianninas A., Bergeron P., Dupuis J., and Ruiz M. T., 2010, *ApJ*, 720, 581
- Hébrard G., Allard N. F., Kielkopf J.F., Chayer P., Dupuis J, Kruk J., Hubeny I, 2003, *A&A*, 405 1153
- Herman, R., & Wallis, R. F. 1956, *Apj*, 123, 353
- Holweger H., Koester D., Allard N. F., 1994, *A&A*, 290, L21
- Holberg J. B., Kruk J. W., Koester D., Barstow M. A., Burleigh M. R., Sahu M. S., 2003, *NATO ASIB Proc. 105: White Dwarfs*, 113
- Hylleraas E. A., 1931, *Zeitschrift fur Physik*, 71, 739
- Jaffé G., 1934, *Zeitschrift fur Physik*, 87, 535

- Kepler S. O., Castanheira B. G., Costa A. F. M., Koester D., 2006, MNRAS, 372, 1799
- Kepler S. O., Kleinman S. J., Nitta A., Koester D., Castanheira B. G., Giovannini O., Althaus L., 2007, ASP, 372, 35
- Kepler S. O., Kleinman S. J., Pelisoli I., Peçanha V., Diaz M., Koester D., Castanheira B. G., Nitta A., 2010, AIPC, 1273, 19
- Kepler S. O., Nelan E. P., 1993, AJ, 105, 608
- Kielkopf J. F., Allard N. F., Decret A., 2002, European Physical Journal D, 18, 51
- Kleinman S. J., Harris H., Eisenstein D. J., et al., 2004, ApJ, 607, 426
- Kleinman S. J., 2010, AIPC, 1273, 156
- Koester D., 2010, MmSAI, 81, 921
- Koester D., Finley D. S., Allard N. F., Kruk J. W., Kimble R. A., 1996, ApJ, 463, L93
- Koester D., 1991, NATO ASIC Proc. 336: White Dwarfs, 343
- Koester D., Weidemann V., Zeidler-K.T. E. M., Vauclair G., 1985, A&A, 142, L5
- Koester D., Sperhake U., Allard N. F., Finley D. S., Jordan S., 1998, A&A, 336, 276
- Koester D., Sperhake U., Allard N. F., Finley D. S., Jordan S., 1998, A&A, 336, 276
- Koester, D., Kepler, S. O., Kleinman, S. J., & Nitta, A. 2009, Journal of Physics Conference Series, 172, 012006
- Koester D. 2011, private communication
- Kupka F., Piskunov N., Ryabchikova T. A., Stempels H. C., Weiss W. W., 1999, A&AS, 138, 119
- Kupka F. G., Ryabchikova T. A., Piskunov N. E., Stempels H. C., Weiss W. W., 2000, Baltic Astronomy, 9, 590
- Kurucz R., Bell B., 1995, Atomic Line Data, Tech. rep., Cambridge, Mass.: Smithsonian Astrophysical Observatory, 1995.
- Lemke M., 1997, A&A, 122, 285
- Liebert J., Bergeron P., Holberg J. B., 2005, VizieR Online Data Catalog, 215, 60047
- Frommhold L., 1993, Collision-induced Absorption in Gases, Cambridge University Press
- Madsen M. M., Peek J. M., 1971, Atomic Data, 2, 171
- Margenau H., Lewis, M., 1959, Reviews of Modern Physics, 31, 569
- Nelan E. P., Wegner, G., 1985, ApJ, 289, L31
- Piskunov N. E., Kupka F., Ryabchikova T. A., Weiss W. W., Jeffery C. S., 1995, A&AS, 112, 525
- Ramaker D. E., Peek J. M., 1972, Journal of Physics B Atomic Molecular Physics, 5, 2175
- Ramaker D. E., Peek, J. M., 1973, Atomic Data, 5, 167
- Rohrman R. D., Althaus L. G., Kepler S. O., 2011, MNRAS, 411, 781
- Ryabchikova T. A., Piskunov N. E., Kupka F., Weiss W. W., 1997, Baltic Astronomy, 6, 244
- Teller E., 1930, Zeitschrift fur Physik , 61, 458
- Tremblay P.-E., Bergeron P., 2009, ApJ, 696, 1755
- Tremblay, P.-E., Ludwig, H.-G., Steffen, M., Bergeron, P., Freytag, B. 2011, A&AS, 531, L19
- Vennes, S., Chayer, P., Dupuis, J., & Lanz, T. 2005, 14th European Workshop on White Dwarfs, 334, 185
- Vidal C. R., Cooper J., Smith E. W., 1973, ApJ, 25, 37
- Yamamoto N., Kato T., Rosmej F. B., 2004, J. Plasma Fusion Res. SERIES, 6, 748
- Wolff B., Kruk J. W., Koester D., Allard N. F., Ferlet R., Vidal-Madjar A., 2001, A&A, 373, 674
- Zygelman B., Dalgarno A., 1990, ApJ, 365, 239